# Hardware-Efficient CPG Model based on a Ring of Unidirectionally Coupled Oscillators with Perturbation of State Transition Timing

**TAKUMI YOSHIOKA,**
**KENTARO TAKEDA, (Member, IEEE)**
Graduate School of Science for Creative Emergence, Kagawa University, Takamatsu 761-0396 Japan

Corresponding author: Kentaro Takeda (e-mail: takeda@mail.nsci.jp).

**ABSTRACT** A ring of unidirectionally coupled phase oscillators is simple and easy to implement but not suitable for application to central pattern generators (CPGs) owing to the presence of coexisting stable equilibria corresponding to a gait and useless pattern. In this study, we propose a novel approach to applying a ring of unidirectionally coupled phase oscillators to CPGs by incorporating additional circuitry that alters state transition timing. This circuitry comprises a linear-feedback shift register and comparator. Our proposed model successfully generated typical hexapod gait patterns, such as wave and tripod gait patterns, as well as transition patterns between them. The projected Poincarè map was numerically derived to reveal that the proposed model possesses a unique stable equilibrium corresponding to these desired patterns. Furthermore, we implemented the proposed model on a field-programmable gate array (FPGA) to experimentally validate its effectiveness in generating gaits for a hexapod robot. Finally, the proposed model is demonstrated to require fewer FPGA resources compared with conventional and state-of-the-art CPG models.

**INDEX TERMS** Central pattern generator (CPG), coupled oscillators, nonlinear dynamics, synchronization, field-programmable gate array (FPGA), hexapod robot

## I. INTRODUCTION

ALL living organisms constantly produce spatial and temporal biological rhythms for molecular, physiological, or behavioral events [1]. These periodic rhythms can be effectively modeled using nonlinear coupled oscillators owing to their synchronization properties. Examples of such rhythms include circadian rhythm [2]–[4], heart rhythm [5]–[7], and gait rhythm [8]–[27]. The gait rhythm, for example, is believed to be generated by central pattern generators (CPGs), which are neural circuits located in the spinal cord [28], [29]. CPGs have been successfully modeled using nonlinear coupled oscillators, e.g., Van der Pol oscillators [8]–[10], Hopf oscillators [11]–[14], phase (so-called Kuramoto) oscillators [15]–[18], and spiking oscillators [19]–[21]. These models have been successfully applied to generate gait rhythms for various types of neuromorphic robots and clinical prosthetic devices [9]–[27], [30], [31]. A key characteristic of CPGs modeled by nonlinear coupled oscillators is the existence of a unique stable equilibrium corresponding to a specific gait pattern in terms of phase differences. The labeled legs of hexapods and their phase relationships are shown in

Fig. 1(a). A wave gait is characterized by a phase difference of $\pi/3$ between adjacent legs, as shown in the lower left of Fig. 1(a), whereas a tripod gait has a phase difference of $\pi$, as shown in the lower right of Fig. 1(a) [32]. These gaits are supposed to be switched by changing a system parameter. For a model to function as a CPG, its states must converge to a desired phase pattern under steady states, regardless of the initial values. This requirement ensures that the system possesses a unique stable equilibrium. However, nonlinear coupled oscillators lacking this essential characteristic can be easily conceived. Various coupling topologies can be found in a network of oscillators. Here, we focus on recurrent networks where each oscillator is assumed to have one or more pathways to return its outputs to itself. A summary of various types of coupling topologies that are sinusoidally coupled, with over 4-body homogenous phase oscillators and phase difference parameters is shown in Fig. 1(b). The network with the most complex connectivity is of Type (i), whereas the minimum configuration is of Type (iv), which consists of a ring of unidirectionally coupled phase oscillators. Owing to its sparsity of connections, the latter coupled oscillators are expected
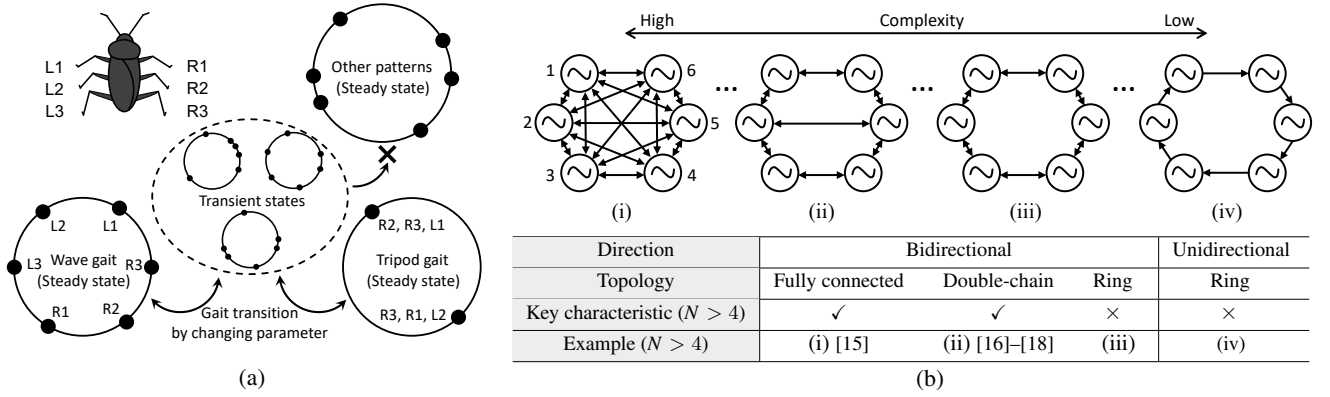
**FIGURE 1.** (a) Key characteristics of the CPG model. The black circles represent the phases of the legs of hexapods. In CPG models, a phase pattern corresponding to a specific gait type, such as wave or tripod gait, must emerge in a stable state regardless of the initial values. Failure to achieve this may result in an undesirable pattern that cannot facilitate gait realization when parameters are adjusted for gait transition. (b) Various coupling topologies involving sinusoidal coupling of over 4-body homogenous phase oscillators with phase difference parameters.

to be efficiently implemented in hardware. However, these coupled oscillators possess coexisting stable equilibria [33], [34] that do not align with the characteristics required for CPG applications.

To address this limitation, a novel CPG model is proposed in this study, which enhances the ring of unidirectionally coupled phase oscillators. In this model, a phase state is randomly perturbed using additional circuitry comprising a linear feedback shift register (LFSR) and comparator. This modification ensures the emergence of a phase pattern necessary for wave and tripod gaits. Furthermore, owing to the sparsity of connections, the proposed model can be implemented with fewer circuit elements in digital hardware compared with those required by a conventional CPG model comprising coupled nonlinear oscillators with a different topology. Other similar solutions include CPG controllers utilizing time delayed couplings of nonlinear oscillators [35]–[40]. For example, based on sophisticated nonlinear analyses, unidirectional ring networks composed of VDP oscillators were successfully designed to produce multiple gait patterns for controlling quadruped and hexapod robots [35], [36]. This methodology was also demonstrated to be applicable to complex networks composed of half-center oscillators in the CPGs of a snake and lobster, with analyses of bifurcations and chaos [37]–[40]. In this study, we compared the proposed model with such a state-of-the-art model in terms of the hardware resources required for implementation.

The remainder of this paper is organized as follows: Section II introduces a ring of unidirectionally coupled phase oscillators. A synchronization metric is introduced to quantitatively evaluate the phase patterns of wave, tetrapod and tripod gaits. The analysis using this metric demonstrates that coupled phase oscillators are not suitable for CPG-based applications. In Section III, a novel CPG model is proposed based on enhancements to the coupled phase oscillators. By using the synchronization metric, the phase patterns of wave, tetrapod, and tripod gaits are validated to be appropriately generated in the proposed CPG model. Additionally, the

projected Poincarè map [41]–[43] is numerically derived to reveal that the model has a unique stable equilibrium corresponding to these gaits, unlike the original model. Section IV examines the implementation of the proposed CPG model on a field-programmable gate array (FPGA). Through an experiment, we validated that a hexapod robot equipped with the FPGA can realize a tripod gait. Furthermore, the proposed CPG model requires fewer FPGA resources compared with the conventional and state-of-the-art CPG models. The findings of this study can contribute to the realization of neuromorphic robots and clinical prosthetic devices with limited circuit scale and power capacity.

Preliminary results can be found in our conference paper in which the fundamental concept explored in this study, coupled phase oscillators with perturbation of state transition timing, was proposed. The significant extensions of this study from the previous work are as follows:

i) The previous model was extended to apply to a CPG of hexapods, which produce primary gait patterns of their kind: wave, tetrapod, and tripod gait patterns.

ii) The extended model was analyzed to demonstrate its stabilities for producing the gait patterns.

iii) It was demonstrated that the extended model was implemented on an FPGA with fewer hardware resources.

iv) It was demonstrated that a hexapod robot driven by the extended model realized the gait patterns properly.

## II. RING OF UNIDIRECTIONALLY COUPLED PHASE OSCILLATORS

We consider the following ring of unidirectionally coupled phase oscillators [33], [34] with a phase difference parameter $\phi \in \mathbf{S}^1 \equiv \{e^{jx} \mid 0 \leq x < 2\pi\}$.

$$\frac{d\theta_i}{dt} = \omega + K\sin(\theta_{i+1} - \theta_i + \phi), \ \ \theta_i \in \mathbf{S}^1, \quad (1)$$

where $i \in \{1, 2, \cdots, N\}$ represents an index of the oscillators with periodic boundary conditions, that is, $\theta_{i+N} \equiv \theta_i$. This study focuses on CPGs of hexapods; thus, $N$ is consistently set to 6 throughout this study. Moreover, these indexes are
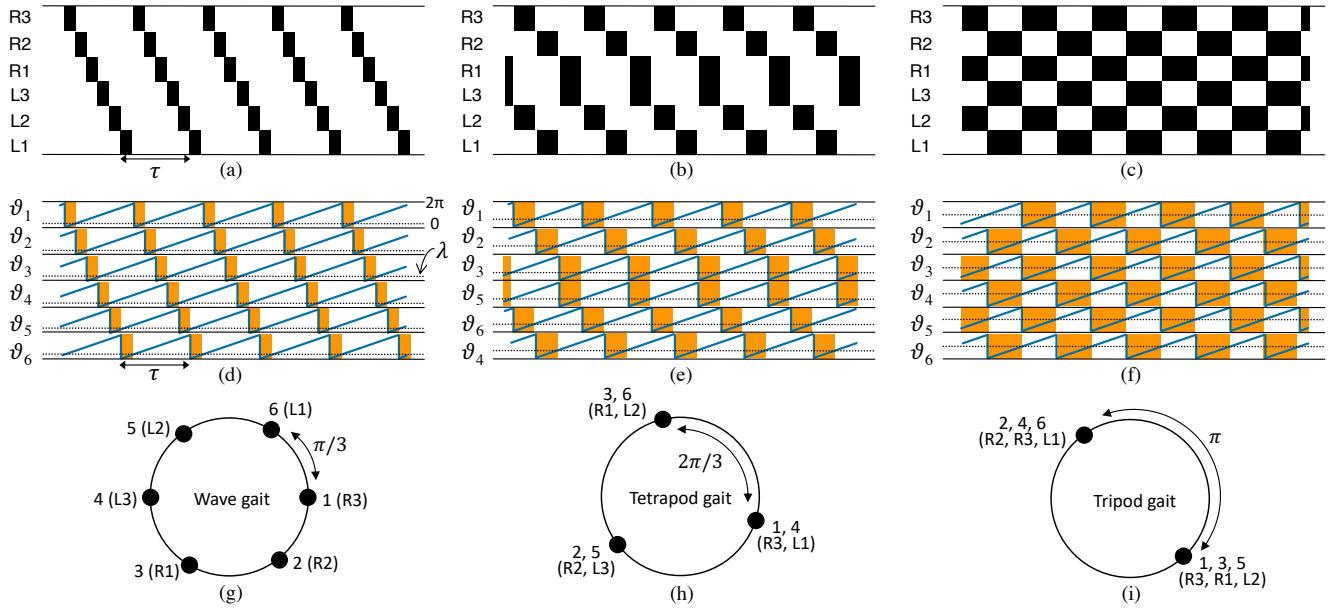
IEEE *Access*



**FIGURE 2.** (a)–(c) Gait diagrams of wave, tetrapod, and tripod gait [32]. (d)–(f) target time waveforms ($\vartheta_1(t), \vartheta_2(t), \cdots, \vartheta_6(t)$) and gait diagrams produced by applying function $\sigma$ to them. (g)–(i) target steady-state phase relationships obtained by time waveforms ($\vartheta_1(t), \vartheta_2(t), \cdots, \vartheta_6(t)$). (d) $\lambda = \pi/3$. (e) $\lambda = 2\pi/3$. (f) $\lambda = \pi$.

associated with the legs of hexapods, as shown in Fig. 1(a). $\omega \in \mathbb{R}^+ \equiv \{x \in \mathbb{R} \mid x > 0\}$ represents the natural angular frequency of each oscillator, whereas $K \in \mathbb{R}^+$ represents the coupling strength. For numerical computation, the coupled oscillators in Eq. (1) are discretized by utilizing the forward Euler method, a straightforward numerical integration technique as follows:

$$\theta_i(t+h) = \theta_i(t) + h\big(\omega + K\sin(\theta_{i+1}(t) - \theta_i(t) + \phi)\big), \quad (2)$$

where $h \in \mathbb{R}^+$ denotes a discretized time step.

Here, we define target steady-state phase relationships to be produced based on observations of hexapod gait diagrams. The diagrams of the primary gait patterns, so-called wave, tetrapod, and tripod gait, are shown in Figs. 2 (a), (b), and (c), respectively [32]. In these diagrams, the leg numbers are associated with the legs of hexapods illustrated in Fig. 1(a). The black rectangle represents the swing phase, when the leg is off the ground and moves forward, and the white region represents the stance phase, when the leg is touching and crawling on the ground. As indicated by the two-way arrow in Fig. 2(a), a pair of the black rectangle and white region forms a period of gait movement represented by $\tau \in \mathbb{R}^+$. Consider reconstructing these gait diagrams from the following target time waveforms with the period $\tau$:

$$\vartheta_i(t) \equiv 2\pi t/\tau + \vartheta_i^0, \quad \vartheta_i \in \mathbf{S}^1, \quad (3)$$

where $\vartheta_i^0 \in \mathbf{S}^1$ is an initial phase. Figs. 2(d), (e), and (f) show examples of the target time waveforms for the three kinds of gait, where the order of $\vartheta_i$ is consistent with that of the leg numbers in Figs. 2(a), (b), and (c). Then, consider the

following function for mapping these time waveforms to gait diagrams:

$$\sigma(\vartheta) \equiv \begin{cases} \text{``orange rectangle''} & \text{for } \vartheta < \lambda, \\ \text{``white region''} & \text{for } \vartheta \geq \lambda, \end{cases}$$

$$\sigma : \mathbf{S}^1 \to \{\text{``orange rectangle''}, \text{``white region''}\},$$

where $\lambda \in \mathbf{S}^1$ represents a threshold parameter to determine the boundary between the "orange rectangle" and the "white region," as indicated by the one-way arrow in Fig. 2(d). The orange rectangles in Figs. 2(d), (e), and (f) show the results by applying the map $\sigma$ to the time waveforms ($\vartheta_1(t), \vartheta_2(t), \cdots, \vartheta_6(t)$). For example, in order for the orange rectangles to match the black rectangles in Figs. 2(a) and (d), the initial phases ($\vartheta_1^0, \vartheta_2^0, \cdots, \vartheta_6^0$) must be set to

$$\varphi_i = \pi/3 \text{ for all } i, \quad \lambda = \pi/3,$$

where

$$\varphi_i \equiv \vartheta_i^0 - \vartheta_{i+1}^0 \pmod{2\pi}, \quad \varphi_i \in \mathbf{S}^1.$$

The resulting phase relationship of ($\vartheta_1(t), \vartheta_2(t), \cdots, \vartheta_6(t)$) is shown in Fig. 2(g). Therefore, to produce the wave gait, we must generate time waveforms ($\theta_1(t), \theta_2(t), \cdots, \theta_6(t)$) that satisfy this phase relationship in a steady state. Similarly, to produce the tetrapod gait and tripod gait, $\varphi_i$ must be set to

$$\varphi_i = 2\pi/3 \text{ for all } i, \quad \lambda = 2\pi/3,$$

$$\varphi_i = \pi \text{ for all } i, \quad \lambda = \pi$$

and the resulting phase relationships are shown in Figs. 2(h) and (i), respectively. Note that in Fig. 2(e), the order of $\vartheta_i$ is changed, i.e., the assignments between the leg numbers and oscillator indices are different for the tetrapod gait.

This article has been accepted for publication in IEEE Access. This is the author's version which has not been fully edited and
content may change prior to final publication. Citation information: DOI 10.1109/ACCESS.2024.3440327

**IEEE** *Access*

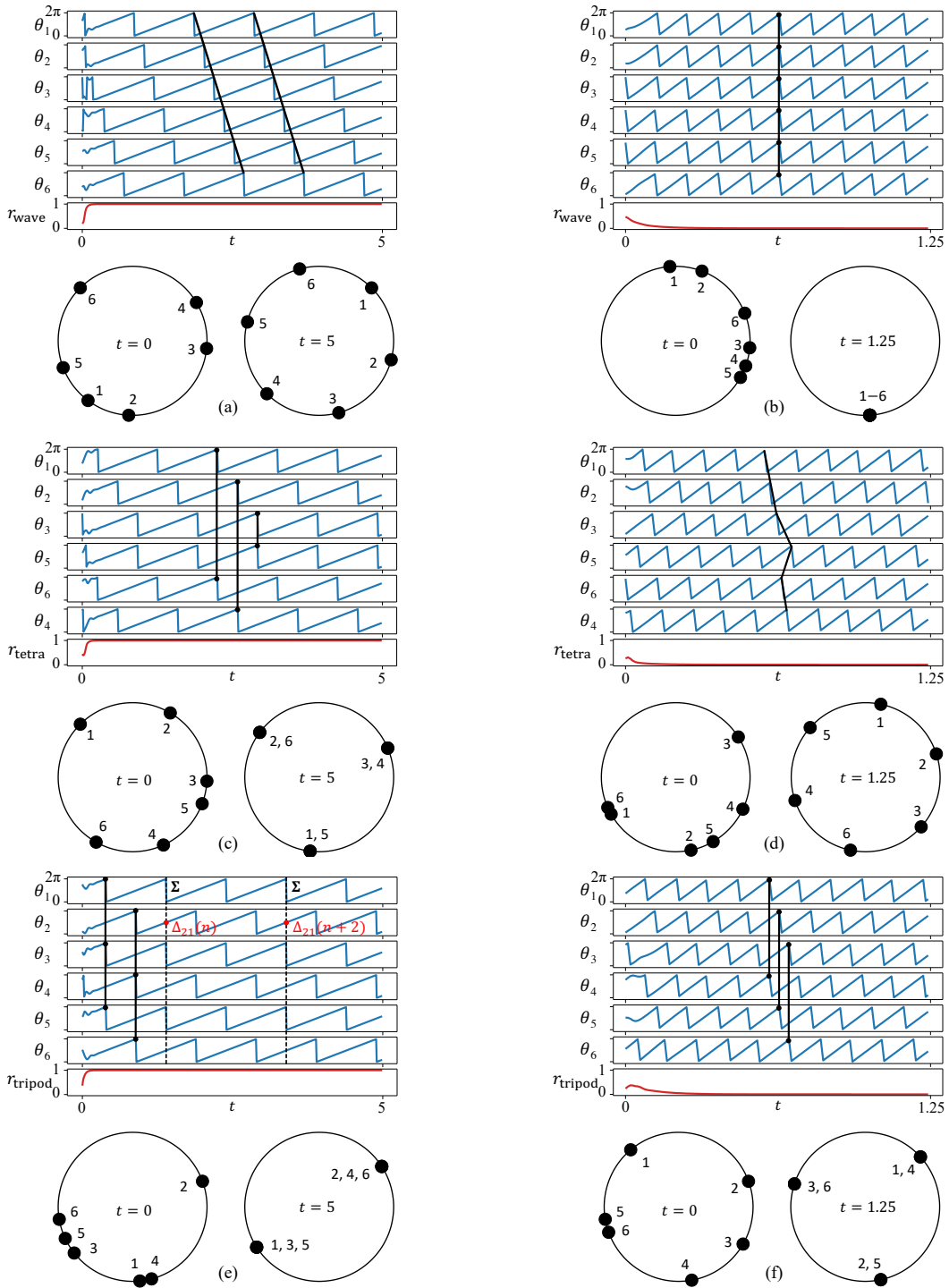Author *et al.*: Preparation of Papers for IEEE TRANSACTIONS and JOURNALS

**FIGURE 3.** (a) Successfully wave gait generation in Eq. (2). Top: Time waveforms of phases $\theta_i$ and synchronization metric $r_{wave}$. Bottom: Initial and steady-state phases at $t = 0$ and at $t = 5$ and $1.25$. The parameter values are expressed as $(\omega, K, \phi, h) = (2\pi, 50, \pi/3, 10^{-2})$. The initial phases are expressed as $(\theta_1(0), \theta_2(0), \cdots, \theta_6(0)) = (4.07, 4.66, 6.18, 0.54, 3.51, 2.35)$. (b) Unsuccessful wave gait generation in Eq. (2). The parameter values are the same as those provided in (a). The initial phases are expressed as $(\theta_1(0), \theta_2(0), \cdots, \theta_6(0)) = (1.65, 1.21, 6.19, 5.94, 5.77, 0.38)$. (c) Successfully tetrapod gait generation in Eq. (2). The parameter values are expressed as $(\omega, K, \phi, h) = (2\pi, 50, 2\pi/3, 10^{-2})$. The initial phases expressed as $(\theta_1(0), \theta_2(0), \cdots, \theta_6(0)) = (2.35, 1.04, 6.23, 5.14, 5.92, 4.2)$. (d) Unsuccessful tetrapod gait generation in Eq. (2). The parameter values are the same as those provided in (c). The initial phases are expressed as $(\theta_1(0), \theta_2(0), \cdots, \theta_6(0)) = (3.66, 4.92, 0.57, 5.84, 5.24, 3.56)$. (e) Successfully tripod gait generation in Eq. (2). The parameter values are expressed as $(\omega, K, \phi, h) = (2\pi, 50, \pi, 10^{-2})$. The initial phases expressed as $(\theta_1(0), \theta_2(0), \cdots, \theta_6(0)) = (4.81, 0.35, 3.81, 4.97, 3.58, 3.31)$. (f) Unsuccessful tripod gait generation in Eq. (2). The parameter values are the same as those provided in (e). The initial phases are expressed as $(\theta_1(0), \theta_2(0), \cdots, \theta_6(0)) = (2.27, 0.35, 5.76, 4.89, 3.31, 3.49)$.
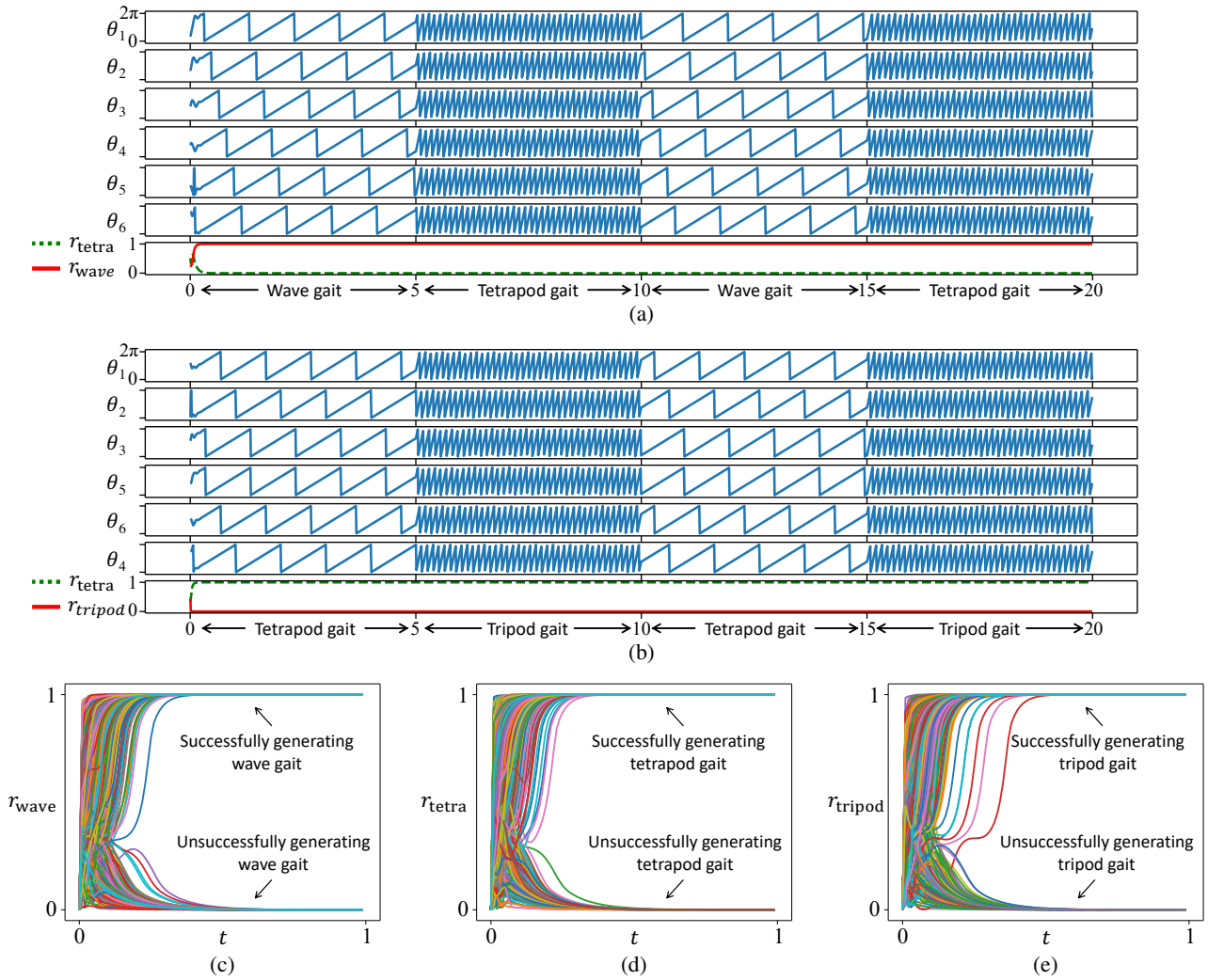
**IEEE** *Access*



**FIGURE 4. Unsuccessful transitions between (a) wave and tetrapod gaits, and (b) tetrapod and tripod gaits. In (a), the gait is changed as $\phi = \pi/3$ for $0 \leq t < 5$ and $10 \leq t < 15$, and $\phi = 2\pi/3$ for $5 \leq t < 10$ and $15 \leq t \leq 20$. In (b), the gait is changed as $\phi = 2\pi/3$ for $0 \leq t < 5$ and $10 \leq t < 15$, and $\phi = \pi$ for $5 \leq t < 10$ and $15 \leq t \leq 20$. The remaining parameter values are expressed as $(\omega, K, h) = (2\pi, 50, 10^{-2})$. Overlaid time waveforms of the synchronization metric (a) $r_{\text{wave}}$, (b) $r_{\text{tetra}}$, and (c) $r_{\text{tripod}}$ for a ring of unidirectionally coupled phase oscillators in Eq. (2), whose initial phases $\theta_i(0)$ are 1,000 uniformly random values. A trajectory converging to 1 indicates the successful generation of a gait pattern. The parameters are consistent with those in Fig. 3.**

The time waveforms of the phases in Eq. (2) and their phase relationships at $t = 0$ and at $t = 5$ and 1.25 are shown in Fig. 3(a), where the phase difference parameter $\phi$ is set as follows:

$$\phi = \pi/3 \quad \text{(wave gait)}.$$

As shown in this figure, the coupled oscillators successfully generate the phase pattern of a wave gait in a steady state (refer to Fig. 1(a)). The phase pattern observed in Fig. 3(a) is referred to as a wave gait pattern hereinafter. The time waveforms of the phases in Eq. (2) for differnt initial phases $(\theta_1(0), \theta_2(0), \cdots, \theta_6(0))$ from those provided in Fig. 3(a), as along with their phase relationships at $t = 0$ and $t = 5$ are shown in Fig. 3(b). The coupled oscillators in Fig. 3(b) generate a phase pattern different from the wave gait pattern observed in Fig. 3(a) in a steady state. This indicates that coupled oscillators fail to generate a wave gait pattern. To quantitatively evaluate the generated pattern, a synchroniza-

tion metric $r_{\text{wave}} \in [0, 1]$, which measures the similarity of the phase relationship to those of a wave gait pattern shown in Fig. 2(g) is introduced as follows:

$$r_{\text{wave}}(t) \equiv \frac{1}{6} \left| \sum_{i=1}^{6} \left( e^{\mathrm{j}\left( \theta_i(t) - i\frac{\pi}{3} \right)} \right) \right|. \tag{4}$$

The related study has employed the difference in normalized time at which membrane potentials reach the pre-given threshold value as phase-lag between neuronal units to analyze spatiotemporal patterns and their transition. This metric allows phase states of membrane potentials to be effectively estimated without complex calculations. On the other hand, in this study, since our model deals directly with phase states, we employed metrics such as Eq. (4) measuring the similarity with the phase relationship in Fig. 2(g), which is the modified version of the order parameter of the Kuramoto model [45]. This metric indicates that the coupled oscillators generate

a wave gait pattern when the synchronization metric $r_{\text{wave}}$ approaches 1. As shown in the bottom of the time waveforms in Figs. 3(a) and (b), $r_{\text{wave}}$ approaches 1 for the former, but not for the latter. Similarly, Figs. 3(c) and (d) demonstrate successful and unsuccessful generations of the phase pattern of a tetrapod gait by the coupled oscillators in a steady state, respectively, where the phase difference parameter $\phi$ is set as

$$\phi = 2\pi/3 \quad \text{(tetra gait)}$$

and the remaining parameters are the same as those provided in Figs. 3(a) and (b). The phase pattern observed in Fig. 3(c) is referred to as a tetrapod gait pattern hereinafter. To quantitatively evaluate the generated pattern, a synchronization metric $r_{\text{tetra}} \in [0, 1]$, which measures the similarity of the phase relationship to those of a tetrapod gait pattern shown in Fig. 2(h) is introduced as follows:

$$r_{\text{tetra}}(t) \equiv \frac{1}{6} \left| \sum_{i \in \{2,5\}} e^{\mathrm{j}\left(\theta_i(t) + 2\pi/3\right)} + \sum_{i \in \{1,4\}} e^{\mathrm{j}\theta_i(t)} + \sum_{i \in \{3,6\}} e^{\mathrm{j}\left(\theta_i(t) - 2\pi/3\right)} \right|. \tag{5}$$

This metric indicates that the coupled oscillators generate a tetrapod gait pattern when the synchronization metric $r_{\text{tetra}}$ approaches 1. As shown in the bottom of the time waveforms in Figs. 3(c) and (d), $r_{\text{tetra}}$ approaches 1 for the former, but not for the latter. An example of gait transitions between the wave and tetrapod gaits is shown in Fig. 4(a). Here, the phase difference parameter alternates between $\phi = \pi/3$ and $\phi = 2\pi/3$ every 5 s. However, after the initial 5 s of generating the wave gait, the coupled oscillators in Eq. (2) are unable to generate the tetrapod gait pattern. Lastly, Figs. 3(e) and (f) demonstrate successful and unsuccessful generations of the phase pattern of a tripod gait by the coupled oscillators in a steady state, respectively, where the phase difference parameter $\phi$ is set as

$$\phi = \pi \quad \text{(tripod gait)}$$

and the remaining parameters are the same as those provided in Figs. 3(a) and (b). The phase pattern observed in Fig. 3(e) is referred to as a tripod gait pattern hereinafter. To quantitatively evaluate the generated pattern, a synchronization metric $r_{\text{tripod}} \in [0, 1]$, which measures the similarity of the phase relationship to those of a tripod gait pattern shown in Fig. 2(i) is introduced as follows:

$$r_{\text{tripod}}(t) \equiv \frac{1}{6} \left| \sum_{i=1}^{3} \left( e^{\mathrm{j}\theta_{2i}(t)} + e^{\mathrm{j}\left(\theta_{2i+1}(t) - \pi\right)} \right) \right|. \tag{6}$$

This metric indicates that the coupled oscillators generate a tripod gait pattern when the synchronization metric $r_{\text{tripod}}$ approaches 1. As shown in the bottom of the time waveforms in Figs. 3(e) and (f), $r_{\text{tripod}}$ approaches 1 for the former, but not for the latter. An example of gait transitions between the tetrapod and tripod gaits is shown in Fig. 4(b). Here, the phase difference parameter alternates between $\phi = 2\pi/3$ and $\phi = \pi$ every 5 s. However, after the initial 5 s of generating the tetrapod gait, the coupled oscillators in Eq. (2) are unable
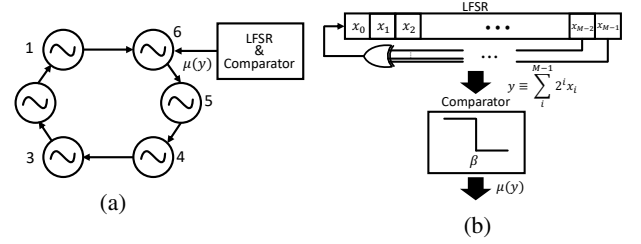


(a)

(b)

**FIGURE 5.** (a) Proposed CPG model, whose dynamics is defined using Eq. (7). The model comprises a ring of unidirectionally coupled phase oscillators with an LFSR and a comparator to randomly update a phase state. (b) LFSR and comparator defined using Eqs. (8)–(10).

to generate the tripod gait pattern. Overlaid time waveforms of the synchronization metrics $r_{\text{wave}}$, $r_{\text{tetra}}$, and $r_{\text{tripod}}$ for 1,000 uniformly random initial phases ($\theta_1(0)$, $\theta_2(0)$, $\cdots$, $\theta_6(0)$) are shown in Figs. 4(c), (d), and (e), respectively. From these figures, initial phases that do not evolve into the wave, tetrapod, and tripod gait patterns were observed.

**Remark 1.** As demonstrated in this section, the ring of unidirectionally coupled phase oscillators exhibits a simple structure but is unsuitable for application to CPGs. Note that the coexistence of stable phase locking solutions in the ring of coupled phase oscillators for $N > 4$ is theoretically guaranteed [33], [34]. To address this limitation, a novel CPG model that enhances the coupled oscillators is proposed in the next section.

## III. RING OF UNIDIRECTIONALLY COUPLED PHASE OSCILLATORS WITH PERTURBATION OF STATE TRANSITION TIMING

This section outlines the proposed model, showcasing its ability to accurately generate wave and tripod gait patterns, as well as transition patterns between them. Furthermore, the projected Poincarè map [41]–[43] was numerically derived to reveal that the proposed model possesses a unique stable equilibrium, unlike the original model.

### A. MODEL DESCRIPTION
The proposed CPG model based on a ring of unidirectionally coupled phase oscillators with additional circuitry comprising an LFSR and a comparator is shown in Fig. 5(a). The dynamics of the proposed model, extended to Eq. (2), is as follows:

$$\begin{cases} \theta_i(t+h) = \theta_i(t) + h\left(\omega + K\sin\left(\theta_{i+1}(t) - \theta_i(t) + \phi\right)\right) \text{ for } i \neq 6, \\ \theta_6(t+h) = \theta_6(t) + h\left(\omega + K\sin\left(\theta_1(t) - \theta_6(t) + \phi\right)\right)\mu(y(t)) \end{cases} \tag{7}$$

where the state transition timing of the 6-th oscillator is randomly perturbed by an LFSR and a comparator. The function $\mu: \mathbf{Z}_M \equiv \{0, 1, \cdots, 2^M - 1\} \to \mathbf{B} \equiv \{0, 1\}$ represents the following comparator with threshold parameter $\beta \in [0, 1]$ (refer to Fig. 5(b)):

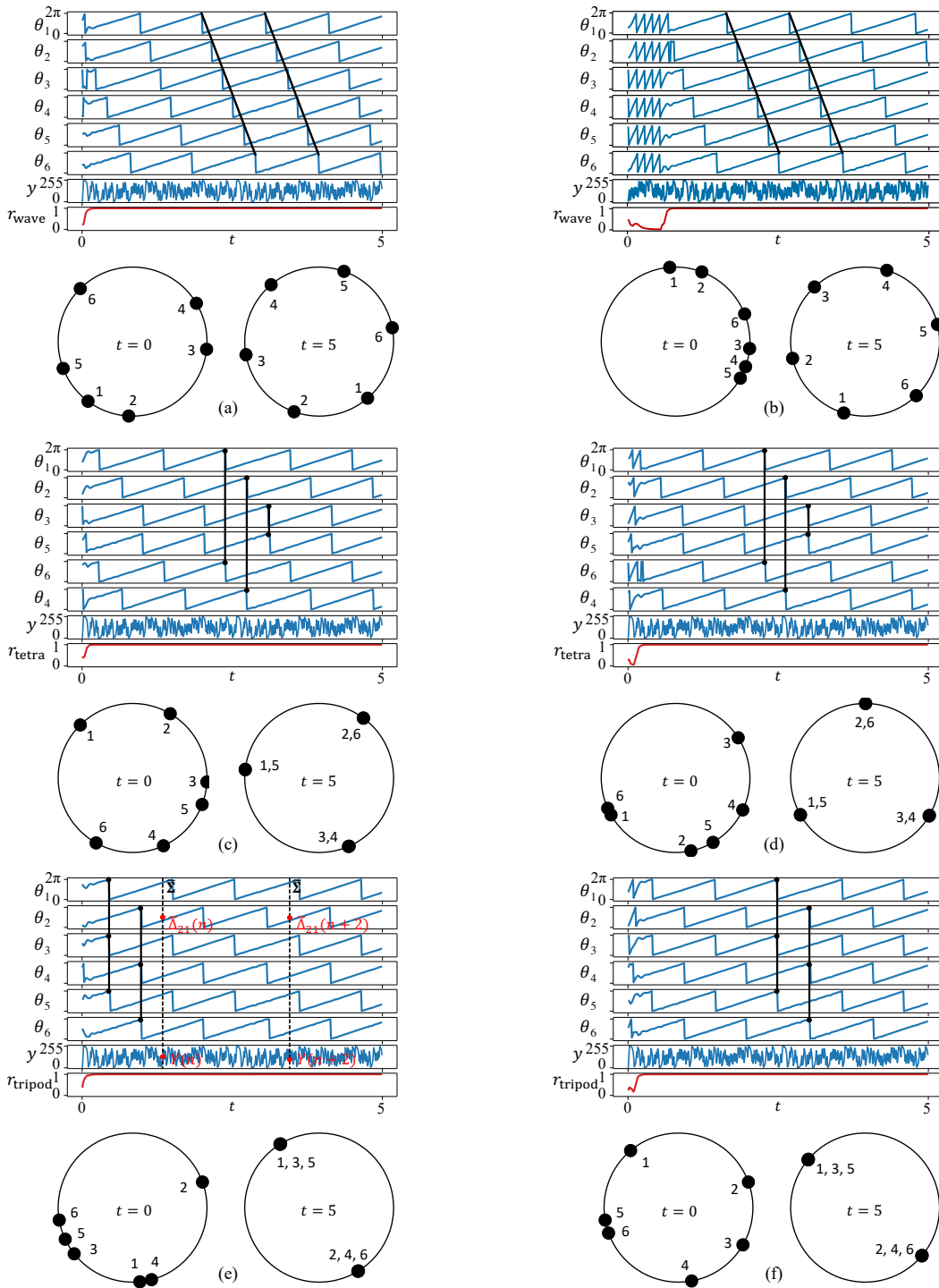$$\mu(y) \equiv \begin{cases} 1 & \text{for } y < \beta, \\ 0 & \text{for } y \geq \beta, \end{cases} \tag{8}$$

This article has been accepted for publication in IEEE Access. This is the author's version which has not been fully edited and
content may change prior to final publication. Citation information: DOI 10.1109/ACCESS.2024.3440327

Author *et al.*: Preparation of Papers for IEEE TRANSACTIONS and JOURNALS

IEEE *Access*

**FIGURE 6.** (a) Successful wave gait generation in Eq. (7). Top: Time waveforms of phases $\theta_i$, state $y$, and synchronization metric $r_{wave}$. Bottom: Initial and steady-state phases at $t = 0$ and $t = 5$. The parameter values are $M = 8$, $\beta = 0.2(2^8 - 1)$, and $a_i = 1$ if $i \in \{3, 4, 5, 7\}$; otherwise, $a_i = 0$. The remaining parameters and phases are the same as those in Fig. 3(a). (b) Successful wave gait generation in Eq. (7). The parameter values are the same as those provided in (a), whereas the initial phases are the same as those provided in Fig. 3(b). (c) Successful tetrapod gait generation in Eq. (7). The parameter values are $M = 8$, $\beta = 0.2(2^8 - 1)$, and $a_i = 1$ if $i \in \{3, 4, 5, 7\}$; otherwise, $a_i = 0$. The remaining parameters and initial phases are the same as those in Fig. 3(c). (d) Successful tetrapod gait generation in Eq. (7). The parameter values are the same as those provided in (c). The initial phases are the same as those provided in Fig. 3(d). (e) Successful tripod gait generation in Eq. (7). The parameter values are $M = 8$, $\beta = 0.2(2^8 - 1)$, and $a_i = 1$ if $i \in \{3, 4, 5, 7\}$; otherwise, $a_i = 0$. The remaining parameters and initial phases are the same as those in Fig. 3(e). (f) Successful tripod gait generation in Eq. (7). The parameter values are the same as those provided in (e). The initial phases are the same as those provided in Fig. 3(d).
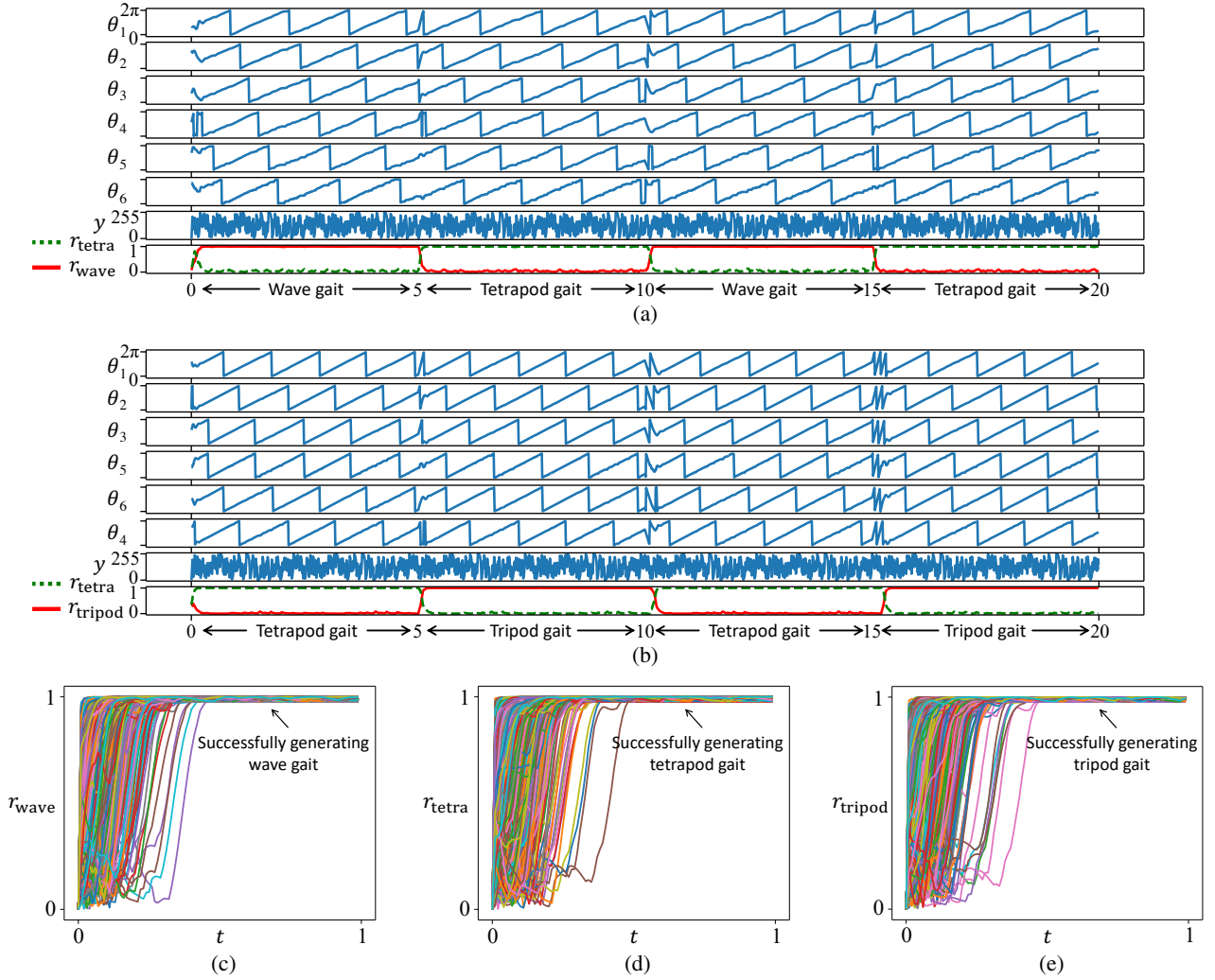
**FIGURE 7.** (a) Successful gait transitions between wave and tetrapod gaits. (b) Successful gait transitions between tetrapod and tripod gaits. Overlaid time waveforms of the synchronization metric (a) $r_{\text{wave}}$, (b) $r_{\text{tetra}}$, and (c) $r_{\text{tripod}}$ defined using Eqs. (4), (5), and (6) for the proposed model in Eqs. (7)–(10), whose initial phases $\theta_i(0)$ are 1,000 uniformly random values. A trajectory converging to 1 indicates the successful generation of a gait pattern. The parameter values are the same as those provided in Fig. 6.

where $M \in \mathbb{N}$ and $\mathbb{N}$ denote a set of positive integers. In addition, $y \in \mathbf{Z}_M$ represents an $M$-bit non-negative integer defined as follows:

$$y(t) \equiv 2^0 x_0(t) + 2^1 x_1(t) + \cdots + 2^{M-1} x_{M-1}(t) \quad (9)$$

where $x_j \in \{0, 1\}$ denotes the binary states of the LFSR (refer to Fig. 5(b)). The dynamics of the binary states $x_j \in \mathbf{B}$ is described as follows:

$$\begin{cases} x_0(t+h) = \big(a_0 x_0(t) + a_1 x_1(t) + \cdots + a_{M-1} x_{M-1}(t)\big) \bmod 2, \\ x_j(t+h) = x_{j-1}(t) \ \text{for} \ j \neq 0, \end{cases}$$
$$(10)$$

where $j \in \{0, 1, \cdots, M-1\}$ denotes an index of the registers, $M$ represents the number of the registers, and $a_j \in \mathbf{B}$ denotes a feedback parameter of the $j$-th register. The parameter $a_j$ is chosen such that the LFSR generates an M-sequence [46]. In addition, the initial values of the LFSR are assumed to be non-zero. The wave gait patterns successfully generated by

utilizing the proposed model in Eq. (7) are shown in Figs. 6(a) and (b). Note that the initial phases in Figs. 6(a) and (b) are the same as those in Fig. 3(a) and (b), respectively. As shown in Fig. 6(b), the proposed model generates, for $0 \leq t \lesssim 0.75$, a distinct phase pattern as shown in Fig. 3(b). However, for $t \gtrsim 0.75$, the generated pattern in the proposed model was entrained to the wave gait pattern without alterations in parameters or additional input signals. The phase relationship at $t = 5$ in this figure is identical to that of Fig. 3(a) (refer to Fig. 1). This entrainment can be also seen in $r_{\text{wave}}$ at the bottom of the time waveforms in Fig. 6(b). Similarly, the successful generations of the tetrapod and tripod gait patterns using the proposed model in Eq. (7) are shown in Figs. 6(c), (d), (e), and (f). Furthermore, examples of gait transitions of the proposed model in Eq. (7) are shown in Figs. 7(a) and (b), according to which the phase difference parameter alternates between $\phi = \pi/3$ and $2\pi/3$ and $\phi = 2\pi/3$ and $\pi$ every 5 s. Unlike Figs. 4(a) and (b), the proposed model can generate

the desired gait patterns for all $t$. Thus, we can infer from these figures that the proposed model achieved gait transitions between wave, tetrapod, and tripod gaits. Overlaid time waveforms of the synchronization metrics $r_{\text{wave}}$, $r_{\text{tetra}}$, and $r_{\text{tripod}}$ for 1,000 uniformly random initial phases $(\theta_1(0), \theta_2(0), \cdots, \theta_6(0))$ in the proposed model are shown in Figs. 7(c), (d), and (e). All initial phases evolved into a wave and tripod gait pattern, respectively.

### B. MODEL ANALYSIS

To compare the stability characteristics with the proposed model, we first derived the projected Poincarè map [41]–[43] of a ring of unidirectionally coupled phase oscillators in Eq. (2). The oscillators have the following whole state space:

$$\mathbf{T}^6 \equiv \underbrace{\mathbf{S}^1 \times \cdots \times \mathbf{S}^1}_{6}. \tag{11}$$

Suppose $\Sigma$ be the following subset of $\mathbf{T}^6$, representing the Poincaré section:

$$\Sigma \equiv \{(\theta_1, \theta_2, \cdots, \theta_6) \in \mathbf{T}^6 \mid \theta_1 = 0\}. \tag{12}$$

The black vertical dashed lines in Fig. 3(c) indicate examples of the Poincaré section $\Sigma$. Therefore, the following state variables sampled on the Poincaré section $\Sigma$ are defined as follows:

$$\Delta_{i1}(n) \equiv \theta_i|_{\theta_1=0} \text{ for } i \in \{2, 3, \cdots 6\}, \ n \in \mathbb{N}, \tag{13}$$

where $\Delta_{i1}(n)$ denotes a phase difference between $\theta_i$ and $\theta_1$ sampled on the Poincaré section $\Sigma$ at $n$-th time. The red circles in Fig. 3(a) indicate examples of $\Delta_{i1}(n)$. The dynamics of $\Delta_{i1}$ are described using the Poincaré map $P : \mathbf{T}^5 \to \mathbf{T}^5$ as follows:

$$\boldsymbol{\Delta}_1(n+1) = P(\boldsymbol{\Delta}_1(n)), \tag{14}$$

where $\boldsymbol{\Delta}_1(n) \equiv (\Delta_{21}(n), \Delta_{31}(n), \cdots, \Delta_{61}(n))$. The repeated composition of this map with itself is defined as the iterated map $P^m : \mathbf{T}^5 \to \mathbf{T}^5$ as follows:

$$\boldsymbol{\Delta}_1(n+m) = P^m(\boldsymbol{\Delta}_1(n)) \equiv \underbrace{(P \circ \cdots \circ P)}_{m}(\boldsymbol{\Delta}_1(n)), \tag{15}$$

where $m \in \mathbb{N}$. Owing to the high dimensionality of the map, understanding its characteristics can be challenging. Therefore, using $P^m$, the following projected Poincaré map can be defined as follows:

$$\mathcal{P}_i^m(\Delta_{i1}(n)) \equiv \{\Delta_{i1}(n+m) \in \mathbf{S}^1 \mid \\ (\Delta_{21}(n+m), \cdots, \Delta_{i1}(n+m), \cdots, \Delta_{61}(n+m)) \\ = P^m((\Delta_{21}(n), \cdots, \Delta_{i1}(n), \cdots, \Delta_{61}(n))), \\ \Delta_{j1}(n) \in \mathbf{S}^1 \text{ for } j \neq i\}. \tag{16}$$

Note that, owing to the complexity of deriving an exact expression of $\mathcal{P}_i^m(\Delta_{i1})$, these values have been numerically calculated using Eq. (2). The projected Poincaré map $\mathcal{P}_2^m(\Delta_{21})$ for a tripod gait pattern of a ring of unidirectionally coupled phase oscillators, where $m = 1$ and $m = 5$ are shown in Fig. 8(a) and (b), respectively. The variable $\Delta_{21}$ represents
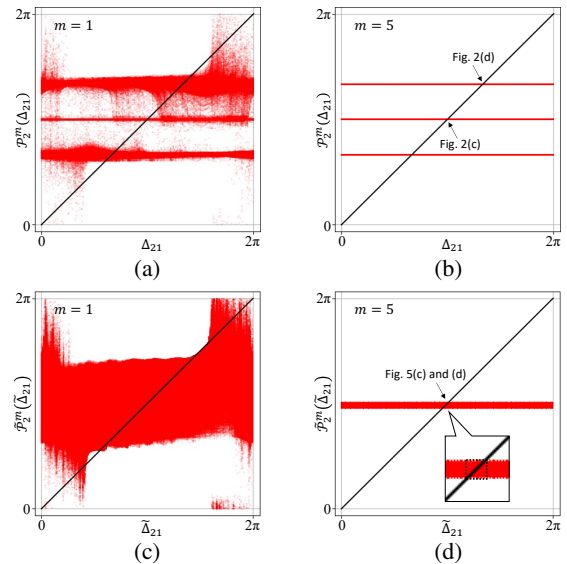


**FIGURE 8.** (a), (b) Projected Poincaré map $\mathcal{P}_2^m$ for a tripod gait pattern of a ring of unidirectionally coupled phase oscillators in Eq. (2). (a) $m = 1$. (b) $m = 5$. The parameter values are the same as those provided in Fig. 3(c) and (d). (c), (d) Projected Poincaré map $\tilde{\mathcal{P}}_2^m$ for a tripod gait pattern of the model presented in Eqs. (7)–(10). (c) $m = 1$. (d) $m = 5$. The parameter values are the same as those provided in Fig. 6(c) and (d).

the phase difference between $\theta_2$ and $\theta_1$, indicating the phase difference between the first and second legs immediately after the first leg swings $m$ times. Therefore, the correct phase difference is $\pi$ for a tripod gait pattern (refer to Fig. 1(a)). In Fig. 8(a), the wide range of values of $\mathcal{P}_2^1(\Delta_{21})$ for any $\Delta_{21}$, renders the evaluation of the exact trajectories and fixed points impossible. Conversely, three distinct horizontal lines can be observed in Fig. 8(b). The exact trajectories cannot be evaluated still; however, the coexisting fixed points can be guessed. That is

$$2\pi/3 \in \mathcal{P}_2^{10}(2\pi/3), \ \ \pi \in \mathcal{P}_2^{10}(\pi), \ \ 4\pi/3 \in \mathcal{P}_2^{10}(4\pi/3).$$

As indicated using arrows in Fig. 8(b), the fixed points $\pi$ and $4\pi/3$ correspond to the patterns in Figs. 3(c) and (d), and were assumed to be stable. These observations can be justified using the theoretical stability analysis method [33], [34]; however, its application to the proposed model is infeasible. Therefore, the projected Poincarè map of the proposed model must be derived to observe its stability characteristics.

Next, we derive the projected Poincarè map of the proposed model in Eqs. (7)–(10). To distinguish this map from the previous one, all mathematical symbols representing variables, functions, and sets are accented with a tilde. The proposed model has the following whole state space:

$$\tilde{\mathbf{T}}^6 \equiv \{(\theta_1, \theta_2, \cdots, \theta_6, y) \in \mathbf{T}^6 \times \mathbf{Z}_M\}. \tag{17}$$

Note that the state variable $y$ of the LFSR is included this time. Let $\tilde{\Sigma}$ represents the following subset of $\tilde{\mathbf{T}}^6$, which represents the Poincaré section:

$$\tilde{\Sigma} \equiv \{(\theta_1, \theta_2, \cdots, \theta_6, y) \in \tilde{\mathbf{T}}^6 \mid \theta_1 = 0\}. \tag{18}$$

In Fig. 6(c), the black vertical dashed lines indicate examples of the Poincaré section $\tilde{\Sigma}$. Therefore, the state variables sampled on the Poincaré section $\tilde{\Sigma}$ are defined as follows:

$$\begin{cases} \tilde{\Delta}_{i1}(n) \equiv \theta_i|_{\theta_1=0} \text{ for } i \in \{2, 3, \cdots 6\}, \\ Y(n) \equiv y|_{\theta_1=0}, \end{cases} \quad n \in \mathbb{N}, \quad (19)$$

where $\tilde{\Delta}_{i1}(n)$ represents the phase difference between $\theta_i$ and $\theta_1$ sampled on the Poincaré section $\tilde{\Sigma}$ at the $n$-th time. The red circles in Fig. 6(c) demonstrate examples of $\tilde{\Delta}_{i1}(n)$ and $Y(n)$. The dynamics of $\tilde{\Delta}_{i1}$ and $Y(n)$ are described using the Poincaré map $\tilde{P}: \mathbf{T}^5 \times \mathbf{Z}_M \to \mathbf{T}^5 \times \mathbf{Z}_M$ as follows:

$$\tilde{\mathbf{\Delta}}_1(n+1) = \tilde{P}(\tilde{\mathbf{\Delta}}_1(n)), \quad (20)$$

where $\tilde{\mathbf{\Delta}}_1(n) \equiv (\tilde{\Delta}_{21}(n), \tilde{\Delta}_{31}(n), \cdots, \tilde{\Delta}_{61}(n), Y(n))$. The repeated composition of this map with itself is defined as the iterated map $\tilde{P}^m: \mathbf{T}^5 \times \mathbf{Z}_M \to \mathbf{T}^5 \times \mathbf{Z}_M$ as follows:

$$\tilde{\mathbf{\Delta}}_1(n+m) = \tilde{P}^m(\tilde{\mathbf{\Delta}}_1(n)) \equiv (\underbrace{\tilde{P} \circ \cdots \circ \tilde{P}}_{m})(\tilde{\mathbf{\Delta}}_1(n)), \quad (21)$$

where $m \in \mathbb{N}$. Therefore, using $\tilde{P}^m$, the projected Poincaré map of the proposed model is defined as follows:

$$\begin{aligned} \tilde{\mathcal{P}}_i^m(\tilde{\Delta}_{i1}(n)) &\equiv \{\tilde{\Delta}_{i1}(n+m) \in \mathbf{S}^1 \mid \\ (\tilde{\Delta}_{21}(n+m), &\cdots, \tilde{\Delta}_{i1}(n+m), \cdots, \tilde{\Delta}_{61}(n+m), Y(n+m)) \\ &= \tilde{P}^m((\tilde{\Delta}_{21}(n), \cdots, \tilde{\Delta}_{i1}(n), \cdots, \tilde{\Delta}_{61}(n), Y(n))), \\ &\tilde{\Delta}_{j1}(n) \in \mathbf{S}^1 \text{ for } j \neq i, Y(n) \in \mathbf{Z}_M \setminus \{0\}\}, \end{aligned} \quad (22)$$

where the zero state is excluded from $\mathbf{Z}_M$ as it is not considered an initial value of $Y$ and its trajectory cannot enter this state. Owing to the complexity of deriving an exact expression of $\tilde{\mathcal{P}}_i^m(\tilde{\Delta}_{i1})$, these values are numerically calculated using Eq. (7)–(10). The projected Poincaré map $\tilde{\mathcal{P}}_2^m(\tilde{\Delta}_{21})$ for a tripod gait pattern of the proposed model, where $m = 1$ and $m = 5$ are shown in Fig. 8(c) and (d), respectively. In Fig. 8(c), similar to Fig. 8(a), the wide range of values of $\tilde{\mathcal{P}}_2^1(\tilde{\Delta}_{21})$ for any $\tilde{\Delta}_{21}$ renders the evaluation of the exact trajectories and fixed points impossible. Conversely, a distinct horizontal thick line was observed in Fig. 8(d). Therefore, for all initial states, the phase difference between the first and second legs becomes $\pi$ immediately after the first leg swings 5 times. Subsequently, the trajectory was confined within the dotted box (refer to the magnified inset in Fig. 8(d)). The size of the dotted box represents the slight deviation of the phase difference from $\pi$, likely resulting from perturbations in state transition timing. These findings are consistent across other variables (that is, $\tilde{\Delta}_{i1}$ for $i \neq 1$) and parameter sets for the wave gait pattern. As a result, the proposed model effectively generates both wave and tripod gait patterns, as well as transition patterns between them.

**Remark 2.** As demonstrated in this section, the combination of the LFSR and comparator with the ring of unidirectionally coupled phase oscillators enables the model to robustly generate wave and tripod gait patterns. This robustness is attributed to perturbations in state transition timing, which guides phase

states away from the attraction domain of undesirable patterns toward that of dominant patterns, such as wave and tripod gait patterns. Note that the additional circuitry is straightforward to implement in digital circuits. As demonstrated in the following section, the proposed CPG model can be implemented using fewer circuit elements compared with those required by a conventional CPG model with a typical topology.

## IV. IMPLEMENTATION AND COMPARISON

This section outlines the implementation of the proposed CPG model in a digital circuit using an FPGA. A laboratory experiment was conducted to validate that a hexapod robot controlled using the proposed FPGA-implemented CPG model could move forward using a tripod gait. Furthermore, a conventional and state-of-the-art CPG model was implemented in the same FPGA to compare hardware resource requirements with the proposed CPG model.

### A. FPGA IMPLEMENTATION

The dynamics of the proposed CPG model, as expressed in Eqs. (7)–(10) are encoded at the register transfer level (RTL). The phase variables $\theta_1 \cdots \theta_6$ as well as parameters $h$, $\omega$, and $\phi$ are represented by 32-bit signed vectors encoded as two's complement fixed-point numbers. The sinusoidal function in the coupling term is approximated using a Xilinx IP core that solves a coordinate rotational digital computer (CORDIC) algorithm [47]. The variable $y$ in the LFSR is represented by an $n$-bit unsigned vector and encoded by a non-negative integer that comprises the binary signals $x_0 \cdots x_n$ as defined in Eq. (9). The parameters $a_0 \cdots a_n$ are represented by constant binary signals. State transitions of these variables in Eqs. (7) and (10) are triggered by an internal clock operating at a frequency of $1/h$. The RTL code was synthesized using Xilinx Vivado Design Suite v2022.2, and the generated bitstream file was downloaded into Xilinx FPGA Artix-7 XC7A100T-1CSG324C. A hexapod robot, KMR-M6 Ver.3, composed of an aluminum alloy frame and resin leg components designed by Kondo Kagaku Co., Ltd. is shown in Fig. 9. The FPGA device was mounted on the frame. Each leg of the hexapod robot was equipped with two servomotors, KRS-2552R2HV ICS, providing two degrees of freedom. The $i$-th servomotor around the yaw axis is driven by a pulse-width modulated (PWM) signal of $A\cos(p(\theta_i(t)))$, where

$$p(\theta) \equiv \begin{cases} \pi\lambda^{-1}\theta & \text{for } \theta < \lambda, \\ \pi\left(\frac{\theta-\lambda}{2\pi-\lambda}+1\right) & \text{for } \theta \geq \lambda, \end{cases} \quad q: \mathbf{S}^1 \to \mathbf{S}^1. \quad (23)$$

and $A \in \mathbb{R}^+$. The $i$-th servomotor around the roll axis is driven by a PWM signal of $q(\theta_i(t))$, where

$$q(\theta) \equiv \begin{cases} A & \text{for } \theta < \lambda, \\ -A & \text{for } \theta \geq \lambda, \end{cases} \quad q: \mathbf{S}^1 \to \{A, -A\}. \quad (24)$$

Moreover, these control operations for driving the servomotors were expressed in RTL code and implemented in the FPGA. Snapshots of a tripod gait in the hexapod robot controlled by utilizing the proposed FPGA-implemented CPG
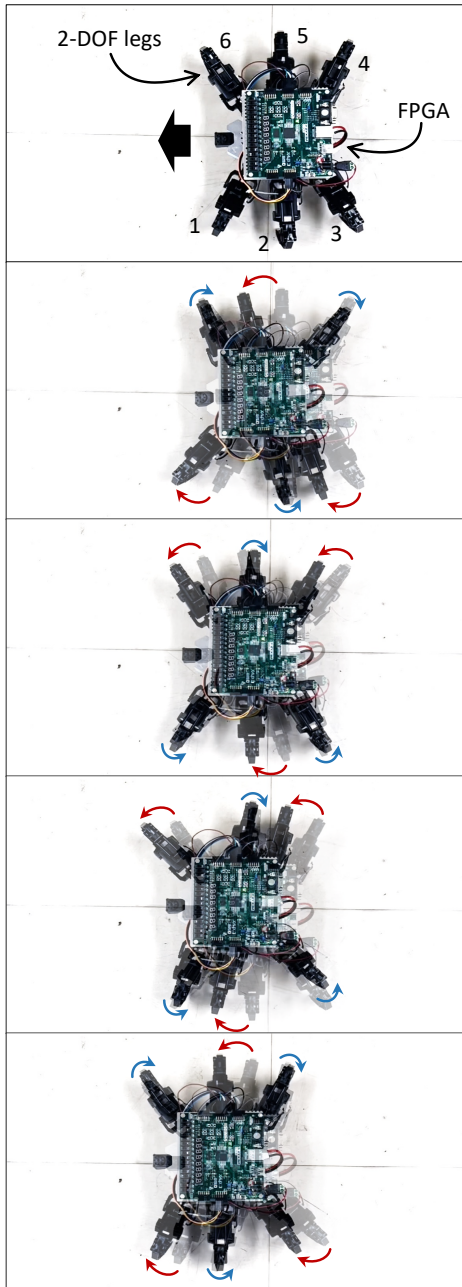
**FIGURE 9.** Snapshots of a tripod gait in the hexapod robot controlled by utilizing the proposed FPGA-implemented CPG model.

model are shown in Fig. 9. As observed, the hexapod robot properly moved forward with a tripod gait.

## B. COMPARISON WITH THE CONVENTIONAL CPG MODEL

Two comparisons of the proposed model were conducted in terms of hardware resources and power consumption against two other models. For the first comparison, a CPG model based on a bidirectional double chain coupling, e.g., [13], [15] was implemented in the same aforementioned FPGA:

$$\frac{d\theta_i}{dt} = \omega + K \sum_{j=1}^{N} k_{i,j} \sin(\theta_j - \theta_i + \phi), \quad (25)$$

**TABLE 1. Comparison results**

|  | **Proposed** | Bidirectional double chain | Time-delayed unidirectional ring |
|---|---|---|---|
| # Slices | **4,447** | 7,114 | 14,646 |
| # LUTs | **14,993** | 24,340 | 24,418 |
| # FFs | **12,462** | 20,277 | 58,331 |
| Power [W] | **0.509** | 0.633 | 1.38 |

Note: Artix-7 XC7A100T-1CSG324C featured 15,850 slices, with each slice containing four 6-input lookup tables (LUTs) and eight flip-flops (FFs). DSP slices and block RAMs were not required. Power consumption figures presented were estimates generated using Xilinx Vivado Design Suite v2022.2. The parameter values of the bidirectional double chain coupling-based CPG were fixed as $(\omega, K, \phi, h) = (2\pi, 2, \pi, 10^{-2})$. The parameter values of the time-delayed unidirectional ring coupling-based CPG were fixed as $(\alpha, \beta, \varepsilon, k, \tau, h) = (1, 1, 0.03, 0.8, 3, 10^{-2})$.

where $i \in \{1, 2, \cdots, 6\}$ represents an index of the oscillators with periodic boundary conditions, that is, $\theta_{i+6} \equiv \theta_i$. The parameters $\omega \in \mathbb{R}^+$ and $\phi \in \mathbf{S}^1$ determine the natural angular frequency and phase difference of each oscillator, whereas $K \in \mathbb{R}$ and $k_{i,j} \in \mathbb{R}$ represent the coupling strength with the coupling structure in Type (ii) of Fig.1(b):

$$\begin{pmatrix} k_{1,1} & \cdots & k_{1,6} \\ \vdots & \ddots & \vdots \\ k_{6,1} & \cdots & k_{6,6} \end{pmatrix} = \begin{pmatrix} 0 & 1 & 0 & 0 & 0 & 1 \\ 1 & 0 & 1 & 0 & 1 & 0 \\ 0 & 1 & 0 & 1 & 0 & 0 \\ 0 & 0 & 1 & 0 & 1 & 0 \\ 0 & 1 & 0 & 1 & 0 & 1 \\ 1 & 0 & 0 & 0 & 1 & 0 \end{pmatrix}. \quad (26)$$

For numerical calculation and digital implementation, the aforementioned bidirectional double chain coupling-based CPG model was discretized using the forward Euler method with a time step $h \in \mathbb{R}^+$. The dynamics of numerical integration formulas for the model in Eq. (25) were also represented through RTL code, following the same methodology as previously outlined. Further, this RTL code was synthesized by utilizing the same design environment software, Xilinx Vivado Design Suite v2022.2. A comparison of the results of the proposed CPG model with those of the bidirectional double chain coupling-based CPG model in terms of required hardware resources and estimated power consumption is shown in Table 1. Based on the results, the proposed CPG model can be implemented with fewer hardware resources and lower power consumption compared with the bidirectional double-chain structure-based CPG model.

For the second comparison, a state-of-the-art CPG model based on a time-delayed unidirectional ring coupling [36] was also implemented in the same aforementioned FPGA:

$$\frac{dx_i(t)}{dt} = y_i(t),$$
$$\frac{dy_i(t)}{dt} = -\varepsilon y_i(t)\left(x_i^2(t) - \alpha\right) - \beta x_i(t) + k\left(y_{i+5}(t-\tau) - y_i(t)\right), \quad (27)$$

where $i \in \{1, 2, \cdots, 6\}$ represents an index of the oscillators with periodic boundary conditions, that is, $\theta_{i+6} \equiv \theta_i$. The parameters $\alpha \in \mathbb{R}^+$, $\beta \in \mathbb{R}^+$, and $\varepsilon \in \mathbb{R}^+$ determine the amplitude, frequency, periodic shape of each oscillator, whereas

$k \in \mathbb{R}^+$ and $\tau \in \mathbb{R}^+$ represent the strength and time delay of coupling, respectively. The time-delayed unidirectional ring coupling-based CPG model has been shown to produce various gaits, such as wave gait, tetrapod gait, and tripod gait, by adjusting the time delay $\tau$ [36]. For numerical calculation and digital implementation, the model was discretized using the forward Euler method with a time step $h \in \mathbb{R}^+$. The dynamics of numerical integration formulas for the model in Eq. (27) were also represented through RTL code, following the same methodology as previously outlined. Further, this RTL code was synthesized by utilizing the same design environment software, Xilinx Vivado Design Suite v2022.2. A comparison of the results of the proposed CPG model with those of the time-delayed unidirectional ring coupling-based CPG model in terms of required hardware resources and estimated power consumption is shown in Table 1. Based on the results, the proposed CPG model can be implemented with fewer hardware resources and lower power consumption compared with the time-delayed unidirectional ring coupling-based CPG model.

**Remark 3.** The reason why the bidirectional double chain coupling-based CPG model and the time-delayed unidirectional ring coupling-based CPG model require more hardware resources than the proposed model is due to the following bottlenecks, respectively: (i) the former has a large number of couplings, resulting it needs to implement many sinusoidal functions, and (ii) while the latter does not use nonlinear coupling functions, it requires numerous registers to store the time delay terms. Note that for fair comparisons, all the model variables were implemented as 32-bit signed vectors.

## V. CONCLUSIONS

This study proposed a novel CPG model based on a ring of unidirectionally coupled phase oscillators with simple additional circuitry that perturbed state transition timing. This additional circuitry included an LFSR and a comparator. Our proposed model could robustly generate wave and tripod gait patterns, as well as a gait transition between them. To validate our findings, we implemented the proposed model on an FPGA and conducted experiments with a hexapod robot. The results demonstrated that the robot, controlled using the FPGA-implemented model, successfully moved forward with a tripod gait. Furthermore, a comparison between our proposed model, the conventional CPG model, and the state-of-the-art CPG model revealed that our model consumed fewer hardware resources for implementation and required less power for operation. These findings suggest that our proposed model is well-suited for neuromorphic robots and clinical prosthetic devices with limited circuit scale and power capacity. Future studies will focus on conducting intensive analyses of synchronization phenomena for parameters of the additional circuitry in the proposed model.

## REFERENCES

[1] E. Kandel *et al.*, *Principles of Neural Science*, 4th ed. McGraw-Hill, New York, 2000.

[2] D. Gonze *et al.*, "Spontaneous Synchronization of Coupled Circadian Oscillators," *Biophys. J.*, vol. 89, no. 1, pp. 120–129, 2005.

[3] S. Bernard *et al.*, "Synchronization-Induced Rhythmicity of Circadian Oscillators in the Suprachiasmatic Nucleus," *PLoS Comput. Biol.*, vol. 3, no. 4, pp. 667–679.

[4] T. Yoshimoto and H. Torikai, "A novel hardware-efficient gene network model based on asynchronous cellular automaton dynamics," *NOLTA, IEICE*, vol. 8, no. 4, pp. 302–318, 2017.

[5] P. E. McSharry *et al.*, "A Dynamical Model for Generating Synthetic Electrocardiogram Signals," *IEEE. Trans. Biomed. Eng.*, vol. 50, no. 3, pp. 289–294, 2003.

[6] S. R.F.S.M. Gois and M. A. Savi, "An analysis of heart rhythm dynamics using a three-coupled oscillator model," *Chaos, Solitons & Fractals*, vol. 41, no. 5, pp. 2553–2565, 2009.

[7] E. Ryzhii and M. Ryzhii, "A heterogeneous coupled oscillator model for simulation of ECG signals," *Comput. Methods Programs Biomed.*, vol. 117, no. 1, pp. 40–49, 2014.

[8] B. Nana and P. Woafo, "Synchronization in a ring of four mutually coupled van der Pol oscillators: Theory and experiment," *Phys. Rev. E*, vol. 74, 2006, Art. no. 046213.

[9] J. H. Barron-Zambrano and C. Torres-Huitzil, "FPGA implementation of a configurable neuromorphic CPG-based locomotion controller," *Neural Netw.*, vol. 45, pp. 50–61, 2013.

[10] H. Yu *et al.*, "Gait Generation with Smooth Transition Using CPG-Based Locomotion Control for Hexapod Walking Robot," *IEEE Trans. Ind. Electron.*, vol. 63, no. 9, pp. 5488–5500, 2016.

[11] W. Chen *et al.*, "Smooth transition between different gaits of a hexapod robot via a central pattern generator algorithm," *J. Intell. Robot. Syst.*, vol. 67, pp. 255–270, 2012.

[12] Y. Hu *et al.*, "Parameter Synthesis of Coupled Nonlinear Oscillators for CPG-Based Robotic Locomotion," *IEEE Trans. Ind. Electron.*, vol. 61, no. 11, pp. 6183–6191, 2014.

[13] Z. Wang *et al.*, "CPG-Inspired Locomotion Control for a Snake Robot Basing on Nonlinear Oscillators," *J. Intell. Robot Syst.*, vol. 85, no. 2, pp. 209–227, 2016.

[14] Z. Cao *et al.*, "Adaptive Path Following and Locomotion Optimization of Snake-Like Robot Controlled by the Central Pattern Generator," *Complexity*, vol. 2019, 2019, Art. no. 8030374.

[15] Y. Zhang *et al.*, "A Novel Double-Layered Central Pattern Generator-Based Motion Controller for the Hexapod Robot," *Mathematics*, vol. 11, no. 3, 2023, Art. no. 617.

[16] A. Crespi and A. J. Ijspeert, "AmphiBot II: An Amphibious Snake Robot that Crawls and Swims using a Central Pattern Generator," *Proc. 9th Int. Conf. Climbing and Walking Robots*, pp. 19–27, 2006.

[17] A. Crespi and A. J. Ijspeert, "Online Optimization of Swimming and Crawling in an Amphibious Snake Robot," *IEEE Trans. Robot.*, vol. 24, no. 1, pp. 75–87, 2008.

[18] J. Wang *et al.*, "Locomotion control of a serpentine crawling robot inspired by central pattern generators," *Proc. 2017 Asia-Pacific Signal and Information Processing Association Annual Summit and Conference (APSIPA ASC)*, pp. 414–419, 2011.

[19] H. Rostro-Gonzalez *et al.*, "A CPG system based on spiking neurons for hexapod robot locomotion," *Neurocomputing*, vol. 170, pp. 47–54, 2015.

[20] E. I. Guerra-Hernandez *et al.*, "A FPGA-Based Neuromorphic Locomotion System for Multi-Legged Robots," *IEEE Access*, vol. 5, pp. 8301–8312, 2017.

[21] P. Lopez-Osorio *et al.*, "Neuromorphic adaptive spiking CPG towards bio-inspired locomotion," *Neurocomputing*, vol. 502, pp. 57–70, 2022.

[22] A. J. Ijspeert, "Central pattern generators for locomotion control in animals and robots: A review," *Neural. Netw.*, vol. 21, no. 4, pp.642–653, 2008.

[23] J. Yu *et al.*, "A survey on CPG-Inspired control model and system implementation," *IEEE Trans. Neural Netw. Learn. Syst.*, vol. 25, no. 441–456, 2014.

[24] K. Takeda and H. Torikai, "A novel hardware-efficient CPG model based on asynchronous cellular automaton," *IEICE Electron. Express.*, vol. 15, no. 1, 2018, Art. no. 20180387.

[25] K. Takeda and H. Torikai, "A Novel Hardware-Efficient Central Pattern Generator Model based on Asynchronous Cellular Automaton Dynamics for Controlling Hexapod Robot," *IEEE Access*, vol. 8, pp. 139609–139624, 2020.

[26] K. Takeda and H. Torikai, "Smooth Gait Transition in Hardware-Efficient CPG Model based on Asynchronous Coupling of Cellular Automaton Phase Oscillators," *NOLTA, IEICE*, vol. 12, no. 3, pp. 336–356, 2021.

[27] K. Takeda, "Analysis of pattern generation in non-periodic clock-driven unidirectionally coupled phase oscillators in a ring," *IEICE Electron. Express.*, vol. 20, no. 13, 2023, Art. no. 20230055.

[28] S. Grillner, "Neurobiological Bases of Rhythmic Motor Acts in Vertebrates," *Science*, vol. 228, no. 4696, pp. 143–149, 1985.

[29] S. Grillner, "The motor infrastructure: from ion channels to neuronal networks," *Nat. Rev. Neurosci.*, vol. 4, pp. 573–586, 2003.

[30] R. R. Torrealba *et al.*, "Cybernetic knee prosthesis: application of an adaptive central pattern generator," *Kybernetes*, vol. 41, no. 1/2, pp. 192–205, 2012.

[31] R. J. Vogelstein *et al.*, "A Silicon Central Pattern Generator Controls Locomotion in Vivo," *IEEE Trans. Biomed. Circuits. Syst.*, vol. 2, no. 3, pp. 212–222, 2008.

[32] D. M. Wilson, Insect walking. *Annu. Rev. Entomol.*, vol. 11, no. 1, pp. 103–122, 1966.

[33] J. A. Rogge and D. Aeyels, "Stability of phase locking in a ring of unidirectionally coupled oscillators," *J. Phys. A: Math. Gen.*, vol. 37, pp. 11135–11148, 2004.

[34] S. Y. Ha and M. J. Kang, "On the Basin of Attractors for the Unidirectionally Coupled Kuramoto Model in a Ring," *SIAM J. Appl. Math.*, vol. 72, no. 5, pp. 1549–1574, 2012.

[35] Z. Song, J. Zhu, and J. Xu, "Gaits generation of quadruped locomotion for the CPG controller by the delay-coupled VDP oscillators," *Nonlinear Dyn.*, vol. 111, pp. 18461–18479, 2023.

[36] Z. Song, J. Zhu, and J. Xu, "Gait Generation of Hexapod Robot for the CPG Controller by Using the Delayed Van der Pol Oscillators," 2023, PREPRINT (Version 1) available at Research Square, doi: 10.21203/rs.3.rs-2539009/v1.

[37] Z. Song, F. Ji, and J. Xu, "Is there a user-friendly building unit to replicate rhythmic patterns of CPG systems? Synchrony transition and application of the delayed bursting-HCO model," *Chaos Solit. Fractals.*, vol. 182, 2024, Art. no. 114820.

[38] Z. Song, X. Huang, and J. Xu, "Spatiotemporal pattern of periodic rhythms in delayed Van der Pol oscillators for the CPG-based locomotion of snake-like robot," *Nonlinear Dyn.*, vol. 110, pp. 3377–3393, 2022.

[39] Z. Song and J. Xu, "Self-/mutual-symmetric rhythms and their coexistence in a delayed half-center oscillator of the CPG neural system," *Nonlinear Dyn.*, vol. 108, pp. 2595–2609, 2022.

[40] Z. Song and J. Xu, "Multi-coexistence of routes to chaos in a delayed half-center oscillator (DHCO) system," *Nonlinear Dyn.*, vol. 112, pp. 1469–1486, 2024.

[41] K. Takeda and H. Torikai, "A Novel Hardware-Efficient Cochlea Model based on Asynchronous Cellular Automaton Dynamics: Theoretical Analysis and FPGA Implementation," *IEEE Trans. Circuits Syst. II: Express Br.* vol. 64, no. 9, pp. 1107–1111, 2017.

[42] K. Takeda and H. Torikai, "A Novel Asynchronous CA Neuron Model: Design of Neuron-like Nonlinear Responses based on Novel Bifurcation Theory of Asynchronous Sequential Logic Circuit," *IEEE Trans. Circuits Syst. I, Reg. Papers* vol. 67, no. 6, pp. 1989–2001, 2020.

[43] K. Takeda and H. Torikai, "Phase-locking phenomena in ergodically coupled CA phase oscillators and its theoretical analysis," *NOLTA, IEICE*, vol. 13, no. 2, pp. 434–439, 2022.

[44] T. Yoshioka, K. Fujimoto, and K. Takeda, "Unidirectionally coupled phase oscillators in a ring with random perturbation," *Proc. 2023 International Symposium on Nonlinear Theory and its Applications (NOLTA)*, pp. 167–168, 2023.

[45] A. Pikovsky, M. Rosenblum, and J. Kurths, *Synchronization: A Universal Concept in Nonlinear Sciences*. Cambridge, U.K.: Cambridge Univ. Press, 2003.

[46] S. W. Golomb and G. Gong, *Signal Design for Good Correlation: For Wireless Communication, Cryptography, and Radar*. Cambridge, U.K.: Cambridge Univ. Press, 2009.

[47] J. E. Volder, "The CORDIC Trigonometric Computing Technique," *IRE Trans. Electronic Computers*, vol. EC-8, no. 3, pp. 330–334, 1959.

**TAKUMI YOSHIOKA** received the Bachelor of Engineering from Kagawa University, Takamatsu, Japan, in 2024. He is currently pursuing the master's degree with the Graduate School of Science for Creative Emergence, Kagawa University. He is a member of IEICE of Japan. His current research interests include bio-inspired robotics.

**KENTARO TAKEDA** (M'18) received the Bachelor of Computer Science and Engineering degree and the Master of Frontier Informatics degree from Kyoto Sangyo University, Kyoto, Japan, in 2017 and 2019, respectively, and the Ph.D. degree in Engineering from Hosei University, Tokyo, Japan, in 2022. He is currently an Assistant Professor with the Faculty of Engineering and Design, Kagawa University, Takamatsu, Japan. He is a member of IEICE of Japan. His current research interests include nonlinear dynamics, neuromorphic computing, machine learning, and digital circuit design.

• • •